

Super-High-Fidelity Image Compression via Hierarchical-ROI and Adaptive Quantization

Jixiang Luo
Sensetime Research

luojixiang@sensetime.com

Yan Wang
Tsinghua University

wangyan@air.tsinghua.edu.cn

Hongwei Qin
Sensetime Research

qinhongwei@sensetime.com

Abstract

Learned Image Compression (LIC) has achieved dramatic progress regarding objective and subjective metrics. MSE-based models aim to improve objective metrics while generative models are leveraged to improve visual quality measured by subjective metrics. However, they all suffer from blurring or deformation at low bit rates, especially at below 0.2bpp. Besides, deformation on human faces and text is unacceptable for visual quality assessment, and the problem becomes more prominent on small faces and text. To solve this problem, we combine the advantage of MSE-based models and generative models by utilizing region of interest (ROI). We propose Hierarchical-ROI (H-ROI), to split images into several foreground regions and one background region to improve the reconstruction of regions containing faces, text, and complex textures. Further, we propose adaptive quantization by non-linear mapping within the channel dimension to constrain the bit rate while maintaining the visual quality. Exhaustive experiments demonstrate that our methods achieve better visual quality on small faces and text with lower bit rates, e.g., **0.7X** bits of HiFiC¹ and **0.5X** bits of BPG.

1. Introduction

Learned Image Compression (LIC) with deep neural networks has gone through rapid development, outperforming traditional methods like JPEG [46] and BPG [3] in terms of objective metrics like Peak Signal-to-Noise Ratio (PSNR) and Multi-scale Structural Similarity (MS-SSIM). The main transformation with hyperprior framework [2, 12, 15, 16, 20, 28–32, 34, 35, 38, 48, 51] models image representation with the constraint of entropy by introducing the concept of Variational AutoEncoder (VAE) [26], acting as the basis of later works which further improve rate-distortion performance. Besides, context is one of the most important modules to provide a more accurate estimate of the proba-

¹<https://hific.github.io/>

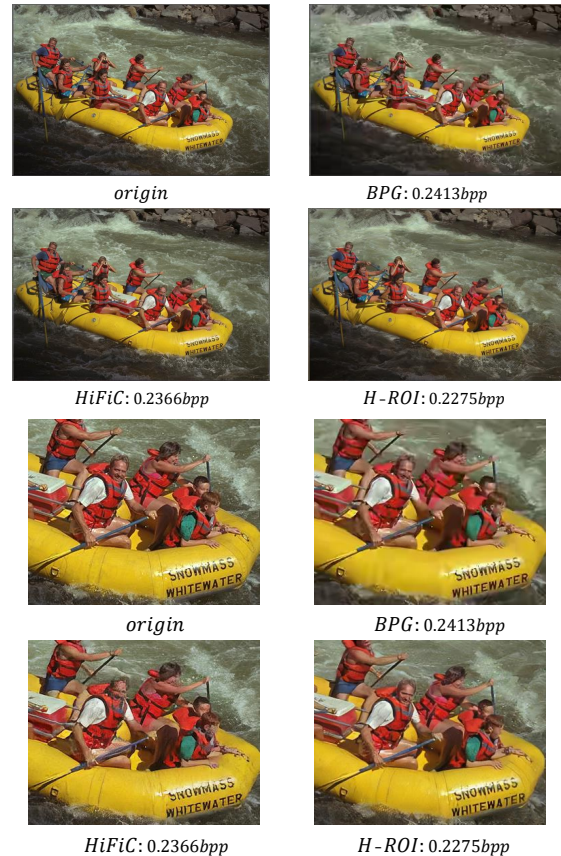


Figure 1. The visual quality of Kodim14 with H-ROI v.s. BPG and HiFiC. Our method shows higher fidelity for human faces and text on the boat with a smaller bpp.

bility of the symbols being encoded by the arithmetic coder. Thus, context models [12, 15, 22, 27, 38] are proposed, utilizing the causality of latent symbols within spatial and channel dimensions. Even though LIC achieves better performance compared to traditional codecs in terms of PSNR and MS-SSIM, LIC still suffers from compression artifacts similar to JPEG compression noise, which is interpreted as



Figure 2. Hierarchical-ROI with a salient object detection network. I is the original image. $F_i, i = 1, 2, 3, B_i, i = 1, 2, 3$ represent the foreground and background of the i_{th} layer. The right column is visualization of salient objects in yellow.

perception-distortion trade-off [4]. Patel et al. [41] proposed deep perceptual compression to align with human eyes using deep perceptual loss. However, adding losses alone is incapable of capturing the characteristics of human eyes. Contour and texture details are still missing at low bit rates.

To obtain better visual perceptual quality of the reconstruction, previous works introduce generative adversarial network (GAN) [18] to enhance perceptual quality by generating more details than those MSE-optimized or MS-SSIM-optimized models. Besides, Agustsson et al. [1] utilize adversarial training to efficiently compress images at low bit rates to maintain details with high frequency. Meanwhile, HiFiC [37] introduces a generator and a conditional discriminator with latents for perceptual quality, resulting in reconstruction more consistent with human eyes. However, they all suffer from common problems caused by GAN, such as unnatural texture, drifted color and some new content from generated noise. Among these phenomena, human faces and text are more sensitive to deformation, especially at low bit rates where small deformation can result in extremely poor visual quality.

Region of Interest (ROI) leverages the importance of image content to allocate bits, assigning enough bits to sophisticated textures to maintain high quality while allocating just a few bits to smooth regions. There exist many excellent works for salient object or region detection [10, 11, 24], which can mark out people, moving objects and other objects with rich colors. Meanwhile, compression with ROI can be categorized into masking on the original image and masking on latents. The works of [6, 40] first utilize a saliency detection network to generate ROI mask, combine it with latents to obtain more efficient image representation, and adjust the quantization step of latents to maintain the most important features. Besides, some methods [7, 8] compress the salient mask using lossless methods along with the latent bitstream to reconstruct facial scenarios at extremely low bit rates, like those below $0.3bpp$. Besides masking latents, Ma et al. [36] also introduce a background

loss and an ROI loss for different image regions. However, all these methods increase computational complexity within the compression process because of additional ROI extracting network.

In this paper, our contribution is threefold:

- We can balance extremely low bit rate and high visual quality, dramatically improving the reconstruction of human faces and text in the foreground, especially for small faces and text. Besides, we further maintain the realism of structure in the background.
- We utilize hierarchical ROI (H-ROI) to split the image into several foreground regions and one background region. Then we apply perceptual loss and GAN loss for the background and apply MSE loss for foregrounds with different importance factors.
- We decouple the adaptive quantization from the ROI mask to make our inference process more efficient by adjusting the quantization boundary with non-linear transformation, which further reduces the bit cost of the background while maintaining visual quality.

2. Background

2.1. LIC with Context Models

Image compression task aims to optimize the rate-distortion function $\mathcal{R} + \lambda\mathcal{D}$, where \mathcal{R} is the bit rate, \mathcal{D} is the distortion, and λ is the Lagrange multiplication factor. Denoting the image as x , encoder and decoder of the neural network as g_a and g_s , the overall loss function is written as follows:

$$\mathcal{L} = \mathbb{E}[-\log p(g_a(x)) + \lambda d(x, g_s(g_a(x)))] \quad (1)$$

where \mathbb{E} is the expectation over $p(x)$, g_a extracts the input image x as latent variable $y = g_a(x)$ and g_s transforms it into reconstructed image \hat{x} .

To eliminate the statistically redundant information, the auto-regressive context model is introduced to promote

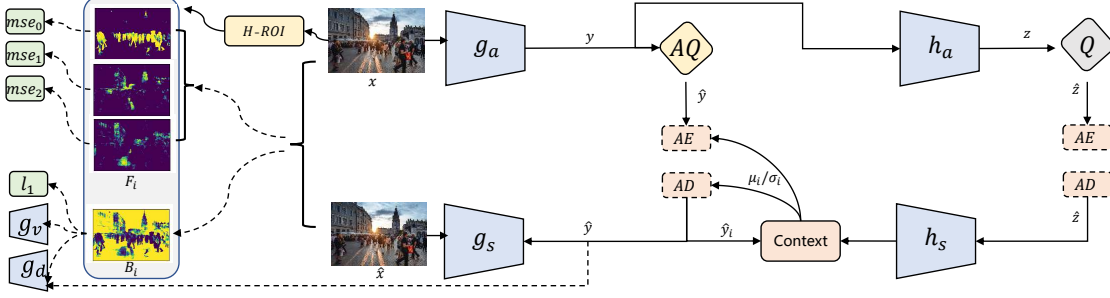


Figure 3. Diagram of the network adopted. The right part is ELIC [21]. We use the same architecture for g_a, g_s, h_a and h_s as the original paper. *Context* denotes the spatial-channel context model described in ELIC. Q, AQ are the quantization and adaptive quantization. AE, AD are the arithmetic encoding and decoding. The left part shows the adversarial training g_d , which has the same discriminator structure as HiFiC [37], and perceptual learning g_v which we train with VGG network [44] and l_1 loss. We use MSE loss $mse_{e_i}, i = 0, 1, 2$ for foregrounds at different levels.

compression performance by leveraging the causality of latents and conceptual similarity. To be specific, the estimation of current symbol $y_{i,j,k}$ can leverage previous symbols $y_{<i,<j,<k}$:

$$p(y_{i,j,k}|y_{<i,<j,<k}) = p(y_{i,j,k}|\Psi(y_{<i,<j,<k})) \quad (2)$$

where i represents the channel dimension and j, k refer to the spatial dimensions. Ψ can be various in combinations of channel or spatial dimensions to construct the context model. Minnen *et al.* [38] utilizes spatial information while [21, 39] use channel context modeling.

2.2. LIC with Generative Adversarial Networks

Some works [9, 17, 37, 42, 47] take image restoration task as image generation, and GAN has been a powerful tool for image generation or style transfer. Meanwhile, g_s can be regarded as a generator, while discriminator g_d is introduced to eliminate the discrepancy between objective metrics and the human visual system. Different from the training of GAN in which generator and discriminator update their weight alternately, g_s, g_a and g_d in the image compression framework with discriminator are jointly trained [37]. To train the discriminator g_d , an auxiliary discriminator loss like binary cross-entropy is introduced:

$$\mathcal{L}_{gan} = -\mathbb{E}[\log g_d(x, \hat{y})] - \mathbb{E}[\log(1 - g_d(\hat{x}, \hat{y}))], \quad (3)$$

where \hat{y} acts as a bridge between the original image and the reconstructed image, improving the visual quality.

2.3. LIC with Salient Object Detection

Spatial and temporal information is essential for salient object detection as it facilitates the detection of human attention. It leverages the binary cross entropy loss between

ground truth and prediction :

$$\mathcal{L}_{bce} = -\frac{1}{N} [m_i \log(p(m_i)) + (1 - m_i) \log(1 - p(m_i))], \quad (4)$$

where N is the total number of pixels, m_i is the ground truth, $p(m_i)$ is the predicted probability.

Then mask m is applied to the latents generated from $g_a(x)$ as described in [6, 36, 40] to modify Eq. 1:

$$\mathcal{L} = \mathbb{E}[-\log p(m \otimes g_a(x)) + \lambda d(x, g_s(m \otimes g_a(x)))], \quad (5)$$

where \otimes is the element-wise operator. The inference process must balance the complexity of salient object detection and rate-distortion performance since the mask m and latents $g_a(x)$ are related in the optimization. Gu *et al.* [19] proposed PCSA which leverages Pyramid structure and Constrained Self-Attention to capture salient objects with various scales. Besides, it can save computation and memory costs by looking at neighbor regions instead of global areas.

3. Architecture

We adopt ELIC [21] framework as our coding architecture. Fig. 3 shows its diagram, which consists of g_a, g_s, h_a, h_s . When optimizing MSE, it achieves better RD performance than VVC [5] w.r.t. both PSNR and MS-SSIM. Q, AQ are the quantization and adaptive quantization. *Context* is the probability engine for AE, AD , which are the arithmetic encoder and decoder. g_d is the discriminator conditioned on latents and y , and g_v is the VGG [44] network we utilize for LPIPS [49] loss. H-ROI is described in Fig. 2. Then, we have the following training loss for the first stage:

$$\mathcal{L}_{stage1} = \mathcal{R} + \lambda_0 * MSE, \quad (6)$$

where \mathcal{R}, MSE are the bit rate and mean square error function. For the second stage, we have the following loss for-

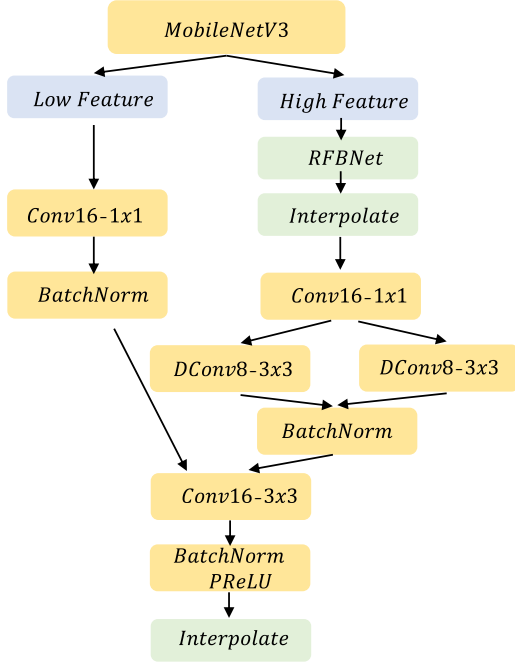


Figure 4. PCSA is simplified from [19] in H-ROI. MobileNetV3 [25] is used to extract low-dimensional and high-dimensional features. *Conv16-1x1* represents the convolutional layer with 1×1 kernel and 16 output channels, while *DConv8-3x3* denotes the dilated convolutional layer with dilation 3 and 8 output channels. *BatchNorm* and *PReLU* are the activation function. *interpolate* denotes the bilinear upsampling.

mulation:

$$\mathcal{L}_{stage2} = \mathcal{R} + \sum_{i=0}^2 [\lambda_i * MSE_i \otimes m_i] + [\lambda_{l_{lips}} * \mathcal{L}_{lips} + \lambda_{l_1} * \mathcal{L}_1 + \lambda_{gan} * \mathcal{L}_{gan}] \otimes (1 - \sum_{i=0}^2 m_i), \quad (7)$$

where $m_i, i = 0, 1, 2$ are the mask generated as shown in Fig. 2 for foregrounds, $\lambda_i, i = 0, 1, 2, \lambda_{lips, gan, l_1}$ are the Lagrange multipliers, and we set $\lambda_0 \geq \lambda_1 \geq \lambda_2$. $\mathcal{L}_{lips, gan, l_1}$ are the LPIPS [49], adversarial and l_1 norm loss function. Besides, $1 - \sum_{i=0}^2 m_i$ represents the mask for the background.

4. Hierarchical-ROI

We apply the salient detection network ψ on original image I to obtain foregrounds $F_i, i = 1, 2, 3$ and backgrounds $B_i, i = 1, 2, 3$:

$$\begin{aligned} F_1, B_1 &= \psi(I) \\ F_2, B_2 &= \psi(B_1) \\ F_3, B_3 &= \psi(B_2) \end{aligned} \quad (8)$$

To obtain the hierarchical attention, we feed the original image into ψ to get the first foreground F_1 and background B_1 . Then, we take B_1 as input and feed it into the same neural network ψ to get F_2, B_2 . The detailed process is shown in Fig 2. The first foreground consists of people on the street which attract the most attention, while the second and third foregrounds include the tower and sunshine, which are more attractive compared to the background.

Besides, as shown in Fig. 4 we utilize MobileNetV3 [25] as the backbone to accelerate the training process. More specifically, we only use one pre-trained salient detection network to complete all region detection. We obtain the low-dimensional feature from shallow layers of MobileNetV3 and high-dimensional feature from deeper layers. Then, RFBNet [33] is used to process high-dimensional features to enhance the accuracy of detection. Bilinear interpolation is applied since the resolution of high-dimensional features is of smaller size than low-dimensional features. At last, the low-dimensional and the high-dimensional features after going through several convolutional layers, are concatenated and interpolated to match the resolution of the input.

5. Adaptive Quantization

LIC usually utilize uniform quantization to quantize the latents and then encode them with arithmetic coding. We adopt the idea of RDOQ [23] to minimize the magnitude of latents by adjusting the quantization boundary, which further reduces the bit cost of the background while maintaining visual quality. Besides, we leverage adaptive channel-wise quantization described below.

To control the bit rate, we minimize the magnitude of latents to constrain its entropy. Then we have the following equation:

$$\hat{y} = \lfloor [y] + \phi(y - [y]) \rfloor, \quad (9)$$

where $\lfloor * \rfloor, \lceil * \rceil$ represent the floor and the round operator. ϕ is the non-linear function to map the fractions into smaller ranges as shown in Fig. 6:

$$\phi(t) = e^{a*t+b} + c, \quad (10)$$

where a, b, c are the parameters determined by $\phi(0.0) = 0.0, \phi(0.5) = \epsilon, \phi(1.0) = 1.0$. For simplification, ϵ is set to $\{0.45, 0.4, \dots, 0.1\}$. When $\epsilon = 0.0$, adaptive quantization is degenerated to the floor($\lfloor * \rfloor$) function.

We balance the bit rate and visual quality to avoid the performance loss caused by floor quantization, and then adaptive quantization can adapt the image content as it manipulates each channel of latents independently and each channel of latents represents different image contents, like the details with high frequency or low frequency.

To be specific, we obtain the non-linear quantization as shown in Fig. 7. ϵ is chosen from the subset with



Figure 5. The influence of quantization with different layers. $layer_1$ means no adaptive quantization, $layer_2, layer_3, layer_4$ means $\epsilon_1, \epsilon_2, \epsilon_3$ are applied for quantization.

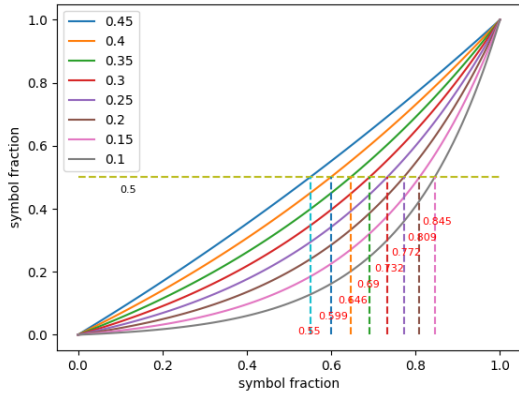


Figure 6. Non-linear mapping. X/Y-axis is the fraction of latents. We map the larger part of the X-axis into the smaller part of the Y-axis. Thus, the original boundary of uniform quantization, which is 0.5, has been changed to the red annotations. And the lines of $\epsilon = \{0.45, 0.4, \dots, 0.1\}$ denote the nonlinearity.

$\{0.4, 0.3, 0.2, 0.1\}$. When ϵ decreases, the range of values quantized to 0 increases and the thresholds which decide symbols to be quantized into the nearest integer above its current value become larger.

We verify the effectiveness of adaptive quantization using the statistical distribution of latents as shown in Fig. 9, which are collected from the CLIC 2022 testing dataset [45] at around $0.2bpp$. The left part is the distribution of the absolute value of y , mostly lying in the range within 10 at the low bit rates. Since almost all previous works adopt uniform quantization with the fraction boundary of 0.5, the right part visualizes the distribution of the fraction of $y - \lfloor y \rfloor$. We shift the threshold value 0.5 to the right as shown in Fig. 6 to $\{0.55, 0.599, \dots, 0.845\}$. By adjusting the boundary, we

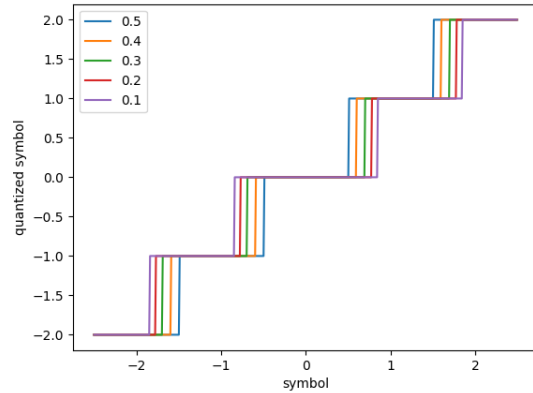


Figure 7. Non-linear quantization. We apply Fig. 6 to both negative and positive fractions to obtain the centrosymmetric quantization range. The quantized symbol 0 has a widened range while other symbols have a range 1 but different quantization boundaries.

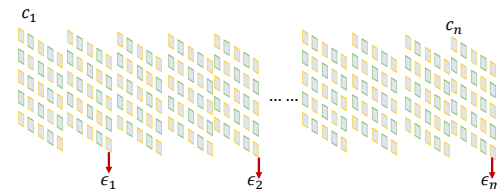


Figure 8. Adaptive quantization with channel groups. c_1, \dots, c_n denote the channels of latents with total number n . For different channel groups, we set $\epsilon_1, \dots, \epsilon_m$ for m channel groups, where $\epsilon_1 \geq \dots \geq \epsilon_m$. The red arrows represent the last channel using ϵ_i .

control the proportion of latents from which 1 is subtracted. To some extent, the proportion is decided by the image con-

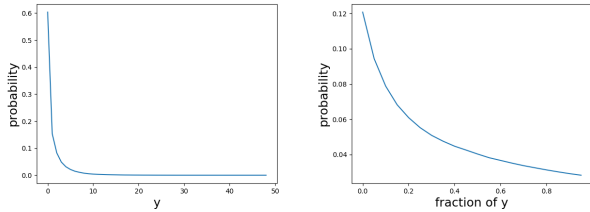


Figure 9. The left part is the statistical distribution of the absolute value of latents y . The right part is the statistical distribution for the fraction $y - \lfloor y \rfloor$ of latents.

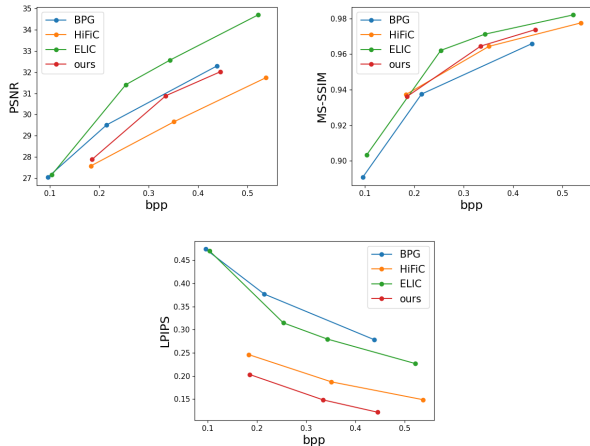


Figure 10. Performance on PSNR, MS-SSIM and LPIPS of our method, HiFiC, ELIC and BPG on Kodak dataset.

text, e.g. some smooth regions require fewer bits. Thus, the corresponding latents can be modified and we can maintain the visual quality while minimizing the bit rate.

6. Experiments

6.1. Training settings

We split the training process into two stages: first, we use MSE loss to train the ELIC models and use the binary cross-entropy loss to train the salient detection network. Then, we fix the weights of the salient detection network and utilize H-ROI to train the framework of ELIC. For the salient detection network, we follow the training setting of PCSA [19].

We use the subset of ImageNet [13] with the number of 8000 in both stages to train ELIC. For the first stage we train 2000 epochs with a learning rate of $1e-4$ and batch size of 2 while for the second stage we train 300 epochs with a learning rate of $5e-5$. Besides, we use learning rate decay with a ratio of 0.9 after every 60 epochs at the second stage to avoid the overfitting caused by perceptual loss and adversarial loss. Meanwhile, we train each model with Adam

optimizer.

For different bit rates we adjust parameter λ in Eq. 1 from the set of $\{3, 8, 15, 200\} \times 10^{-4}$. We first use $\lambda = 200 \times 10^{-4}$ to train one model with an extremely high bit rate, around $1.0bpp$, and then we take it as the basis for other models. We choose the left parameters $\{3, 8, 15\} \times 10^{-4}$ to obtain the models with extremely low bit rates from $0.08bpp$ to $0.3bpp$ on Kodak dataset [14]. We set the total channel number to 320 in Fig. 8 for all models.

It takes about 30 hours with 8 GPUs (Tesla PG503-216) for the training of the first stage, while we only need 6 hours for the second stage. Since we utilize only one pre-trained model of ELIC and PCSA, the total training resource we use is limited.

6.2. Testing settings

We utilize Kodak [14] to evaluate the performance of the codec. To further demonstrate the effectiveness of our method, 30 images selected from the CLIC2022 [45] testing dataset are used and we randomly choose 30 pictures from CrowdHuman [43] testing dataset with 5018 pictures, which consists of various resolutions and numerous scenarios with small faces or text.

6.3. Quantitative Results

Since Zhang *et al.* [50] demonstrates the unreasonable assessment for the objective metrics of visual quality, we utilize PSNR, MS-SSIM and LPIPS [49] for an evaluation more consistent with human eyes to verify the effectiveness of our method. PSNR and MS-SSIM represent fidelity and LPIPS aims to evaluate the realism of images. Thus, we combine these three metrics to measure the performance of codecs to consider both fidelity and reality.

As shown in Tab. 1 and Fig. 10, our method achieves the lowest LPIPS among ELIC, HiFiC and BPG, while maintaining a PSNR close to BPG, and MS-SSIM superior to BPG. To be specific, we calculate LPIPS by PIQ² with normalization in $[0, 1]$ with channels in BGR order. The lower LPIPS is, the better the reconstruction is. Besides we calculate the bit saving to BPG and HiFiC when they achieve the comparable LPIPS. When referring to Kodak dataset in Fig. 10, we obtain more than 50% bits saving over BPG and ELIC, and more than 30% over HiFiC.

6.4. Ablation study

Influence of the Number of Layers for Adaptive Quantization. Fig. 5 demonstrates the effectiveness of adaptive quantization with different channel groups. We set three types of adaptive quantization, each denoted as $layer_2, layer_3, layer_4$ compared to no adaptive quantization, denoted as $layer_1$, where $layer_2$ has two channel

²<https://github.com/photosynthesis-team/piq>

Table 1. Quantitative results with PSNR, MS-SSIM and LPIPS for Kodak, CLIC2022 testing dataset and a subset of CrowdHuman testing dataset

	Kodak				CLIC2022				CrowdHuman Test30			
	bpp	PSNR	MS-SSIM	LPIPS	bpp	PSNR	MS-SSIM	LPIPS	bpp	PSNR	MS-SSIM	LPIPS
BPG	0.0952	27.0262	0.8908	0.4741	0.0888	27.7474	0.9185	0.4443	0.0858	26.7938	0.9258	0.3920
	0.2145	29.5042	0.9375	0.3769	0.1877	30.0832	0.9495	0.3727	0.1730	29.6214	0.9577	0.3005
	0.4383	32.2964	0.9659	0.2782	0.3604	31.9726	0.9642	0.3085	0.3281	32.7234	0.9756	0.2190
ELIC	0.1032	27.1409	0.9033	0.4704	0.1098	27.9678	0.9336	0.4418	0.1375	27.0942	0.9356	0.3899
	0.3426	32.5643	0.9711	0.2797	0.2109	32.0432	0.9703	0.3320	0.2909	31.4825	0.9738	0.2632
	0.5213	34.7049	0.9819	0.2267	0.2809	33.0728	0.9762	0.3052	0.3854	32.6712	0.9796	0.2331
HiFiC	0.1826	27.5647	0.9372	0.2461	0.1518	28.5476	0.9521	0.2338	0.1524	27.5716	0.9555	0.2401
	0.3511	29.6538	0.9643	0.1871	0.2900	30.4707	0.9708	0.1837	0.2898	29.6010	0.9740	0.1845
	0.5377	31.7428	0.9775	0.1484	0.4410	32.2562	0.9799	0.1552	0.4286	31.4336	0.9826	0.1482
ours	0.1854	27.8794	0.9362	<u>0.2028</u>	0.1486	28.5015	0.9510	<u>0.2127</u>	0.1951	27.6499	0.9564	<u>0.2047</u>
	0.3346	30.8858	0.9645	<u>0.1480</u>	0.2707	31.4364	0.9705	<u>0.1822</u>	0.3724	31.0894	0.9766	<u>0.1467</u>
	0.4449	32.0174	0.9737	<u>0.1214</u>	0.3632	32.4728	0.9774	<u>0.1327</u>	0.4860	32.2559	0.9824	<u>0.1226</u>

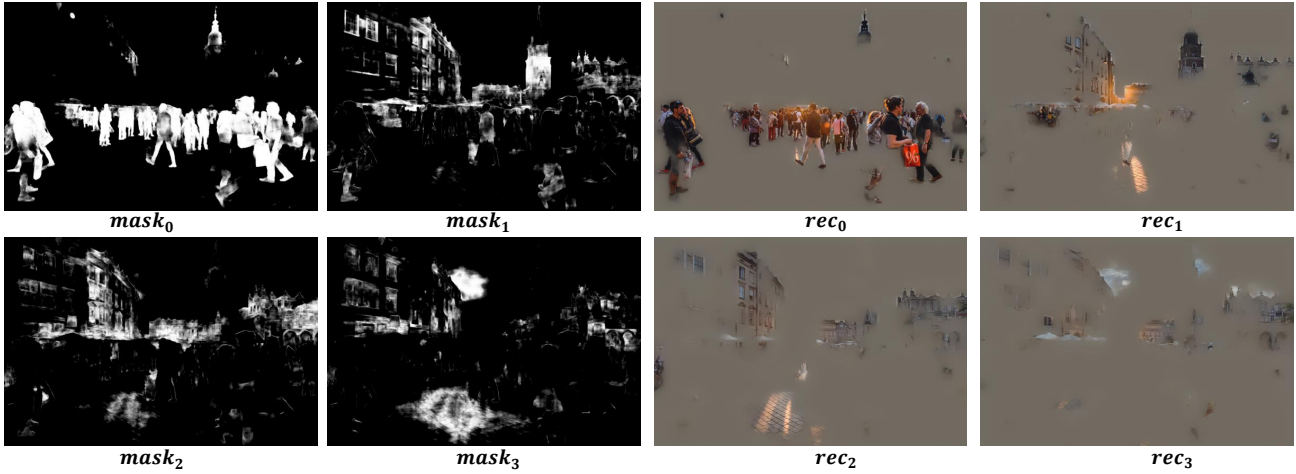


Figure 11. Object coding via applying the ROI masks into the latents. The entangled latents within channel dimensions represent different regions of the image.

groups with 32, 288 channels, $layer_3$ has three groups with 32, 64, 224 channels and $layer_4$ has four groups with 32, 64, 72, 152 channels. When we set more channel groups with larger ϵ_i , the bit rate in Fig. 5 decreases while the fidelity of reconstructed small faces and text is preserved.

For $layer_4$, we set the four groups with $\epsilon_1 = 0.5$, $\epsilon_2 = 0.4$, $\epsilon_3 = 0.3$ and $\epsilon_4 = 0.2$ respectively. The former groups quantize more values to the lower bounds while for the latter group, the opposite is true. Thus, adaptive quantization with channel groups enables progressive coding which improves the visual quality of internal decoding stages as shown in Fig. 12. We restore the images with the former groups $group_i$ and set the latter groups $group_{j>i}$ to zeros. From $group_1$ to $group_4$, the reconstructed image has higher and higher fidelity of color and texture. Meanwhile, the reconstruction of $group_3$ is close to that of $group_4$ because of the low ϵ value of $group_4$.

Mask of H-ROI with Latents for Objective Coding: To demonstrate the effectiveness of H-ROI mask with PCSA, we further apply the mask of H-ROI on latents. Similar to Fig. 8, we split the total c_n channels into several groups, and each group is combined with mask by element-wise multiplication as shown in Eq. 5. We train and infer the network with masks generated by the PCSA network on \hat{y} . To be specific, we only visualize four channels to distinguish the latents with the same channel index $y_{0,i,j}$, $y_{60,i,j}$, $y_{120,i,j}$, $y_{240,i,j}$. Each latent in Fig. 13 (a) consists of all image contents differing only in frequency. While the latents in Fig. 13 (b) are extracted from four different groups split with c_n channels, which distinguish the foreground with human and text, and the background represented by the latents of the right part of Fig. 13 (b). Thus, the latents without mask are region-agnostic and contain the global information generated by convolutional kernel.



Figure 12. Progressive decoding with four groups. We restore the $group_1$ by setting latents of the latter groups $group_{2,3,4}$ to zeros, and $group_2$ by setting $group_{3,4}$ to zero, others analogically.

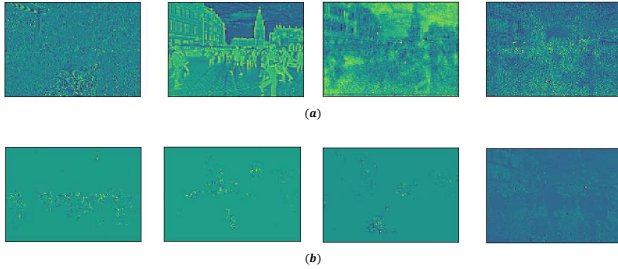


Figure 13. Visualization of latents. The above part (a) is the latents without mask mapping, while (b) shows results of mask mapping with the two-layer ROI. Latents of (a) are region-agnostic while in (b) the first half of channels correspond to the foreground and the second half represents the background.



Figure 14. Ablation study for different layers of H-ROI. Red, yellow and green rectangles represent the regions lying out of the first foreground region F_1 .

While the latents with masks are entangled and hierarchical representations can independently capture different regions,

which is learned by leveraging the ROI mask.

We further utilize the multi-layer ROI masks to reconstruct different regions of images as shown in Fig. 11 with $mask_{0,1,2,3}$ to obtain the reconstruction $rec_{0,1,2,3}$. When we restore one certain region of the image, we set all other channels to zero. Thus the channels of latents can generate corresponding objects for different regions of images.

It is promising to apply the disentangled latents to object detection or segmentation with only the related regions encoded and without other redundant information. Thus, image or video coding for machine can be processed at a very low bit rate. However, coding for machine is beyond the scope of this paper. We leave it as future work.

Influence of the Number of Layers for H-ROI. In our experiments, we utilize four layers as our default settings. We do not consider using more layers because as the number of layers increases, fewer salient objects are detected. As shown in Fig. 11, $rec_{2,3}$ contain fewer regions, and there is no need to increase computation complexity when the gain is negligible.

We compare the reconstructions of Hierarchical-ROI with different numbers of layers with no foreground and 1, 2, 3 layers of foreground and one background. First, we reconstruct them all around $0.16bpp$, and then adjust the number of foregrounds. We obtain images with different visual qualities as shown in Fig. 14. Regions emphasized are marked with red, green and yellow rectangles. For red and yellow regions the reconstruction with $layer_4$ is of higher fidelity without fake textures generated by the adversarial neural network, such as the boundary of brick in the red rectangle and the unnatural color shift noise in the yellow rectangle. Besides, the point in the green rectangle of $layer_4$ is of higher fidelity compared with others.

7. Conclusion

We propose Hierarchical-ROI to detect hierarchical salient regions and maintain image fidelity by applying the MSE loss function with decreasing Lagrange multipliers. Then, we introduce adaptive quantization with non-linear mapping to further reduce the bit rate without compromising visual quality. We maintain the visual quality with bit savings of more than **30%** compared with HiFiC and more than **50%** compared with BPG with regard to LPIPS.

We discuss the concept of objective coding in Sec. 6.4 by combining the mask of H-ROI and latents. The latent is content-aware and we can reconstruct each region independently by setting other channels to zero. It is worth studying for online conferences or meetings by minimizing the bit cost of background. And it can facilitate downstream tasks like object detection since we just need to encode related regions with an extremely low bit rate.

References

- [1] Eirikur Agustsson, Michael Tschannen, Fabian Mentzer, Radu Timofte, and Luc Van Gool. Generative adversarial networks for extreme learned image compression. In *Proceedings of the IEEE/CVF International Conference on Computer Vision*, pages 221–231, 2019. **2**
- [2] Johannes Ballé, David Minnen, Saurabh Singh, Sung Jin Hwang, and Nick Johnston. Variational image compression with a scale hyperprior. *arXiv preprint arXiv:1802.01436*, 2018. **1**
- [3] Fabrice Bellard. Bpg image format. *URL* <https://bellard.org/bpg>, 1:2, 2015. **1**
- [4] Yochai Blau and Tomer Michaeli. The perception-distortion tradeoff. In *Proceedings of the IEEE conference on computer vision and pattern recognition*, pages 6228–6237, 2018. **2**
- [5] Benjamin Bross, Ye-Kui Wang, Yan Ye, Shan Liu, Jianle Chen, Gary J Sullivan, and Jens-Rainer Ohm. Overview of the versatile video coding (vvc) standard and its applications. *IEEE Transactions on Circuits and Systems for Video Technology*, 31(10):3736–3764, 2021. **3**
- [6] Chunlei Cai, Li Chen, Xiaoyun Zhang, and Zhiyong Gao. End-to-end optimized roi image compression. *IEEE Transactions on Image Processing*, 29:3442–3457, 2019. **2, 3**
- [7] Jianhui Chang, Jian Zhang, Youmin Xu, Jiguo Li, Siwei Ma, and Wen Gao. Consistency-contrast learning for conceptual coding. In *Proceedings of the 30th ACM International Conference on Multimedia*, pages 2681–2690, 2022. **2**
- [8] Jianhui Chang, Zhenghui Zhao, Lingbo Yang, Chuanmin Jia, Jian Zhang, and Siwei Ma. Thousand to one: Semantic prior modeling for conceptual coding. In *2021 IEEE International Conference on Multimedia and Expo (ICME)*, pages 1–6. IEEE, 2021. **2**
- [9] Y. Chen, Q. Yuan, X. wu, Z. Zhang, and Y. Feng. Mcm: Multi-channel context model for entropy in generative image compression. In *4th Challenge on Learned Image Compression*, Jun 2021. **3**
- [10] Zuyao Chen, Qianqian Xu, Runmin Cong, and Qingming Huang. Global context-aware progressive aggregation network for salient object detection. In *Proceedings of the AAAI conference on artificial intelligence*, volume 34, pages 10599–10606, 2020. **2**
- [11] Ming-Ming Cheng, Niloy J Mitra, Xiaolei Huang, Philip HS Torr, and Shi-Min Hu. Global contrast based salient region detection. *IEEE transactions on pattern analysis and machine intelligence*, 37(3):569–582, 2014. **2**
- [12] Zhengxue Cheng, Heming Sun, Masaru Takeuchi, and Jiro Katto. Learned image compression with discretized gaussian mixture likelihoods and attention modules. In *Proceedings of the IEEE/CVF Conference on Computer Vision and Pattern Recognition*, pages 7939–7948, 2020. **1**
- [13] Jia Deng, Wei Dong, Richard Socher, Li-Jia Li, Kai Li, and Li Fei-Fei. Imagenet: A large-scale hierarchical image database. In *2009 IEEE conference on computer vision and pattern recognition*, pages 248–255. Ieee, 2009. **6**
- [14] Rich Franzen. Kodak lossless true color image suite. Available: <http://r0k.us/graphics/kodak>, 4(2), 1999. **6**
- [15] Haisheng Fu, Feng Liang, Jianping Lin, Bing Li, Mohammad Akbari, Jie Liang, Guohe Zhang, Dong Liu, Chengjie Tu, and Jingning Han. Learned image compression with discretized gaussian-laplacian-logistic mixture model and concatenated residual modules. *arXiv preprint arXiv:2107.06463*, 2021. **1**
- [16] Ge Gao, Pei You, Rong Pan, Shunyuan Han, Yuanyuan Zhang, Yuchao Dai, and Hojae Lee. Neural image compression via attentional multi-scale back projection and frequency decomposition. In *Proceedings of the IEEE/CVF International Conference on Computer Vision*, pages 14677–14686, 2021. **1**
- [17] S. Gao, Y. Shi, T. Guo, Z. Qiu, Y. Ge, Z. Cui, Y. Feng, J. Wang, and B. Bai. Perceptual learned image compression with continuous rate adaptation. In *4th Challenge on Learned Image Compression*, Jun 2021. **3**
- [18] Ian Goodfellow, Jean Pouget-Abadie, Mehdi Mirza, Bing Xu, David Warde-Farley, Sherjil Ozair, Aaron Courville, and Yoshua Bengio. Generative adversarial nets. *Advances in neural information processing systems*, 27, 2014. **2**
- [19] Yuchao Gu, Lijuan Wang, Ziqin Wang, Yun Liu, Ming-Ming Cheng, and Shao-Ping Lu. Pyramid constrained self-attention network for fast video salient object detection. In *Proceedings of the AAAI Conference on Artificial Intelligence*, 2020. **3, 4, 6**
- [20] Zongyu Guo, Zhizheng Zhang, Runsen Feng, and Zhibo Chen. Causal contextual prediction for learned image compression. *IEEE Transactions on Circuits and Systems for Video Technology*, 32(4):2329–2341, 2021. **1**
- [21] Dailan He, Ziming Yang, Weikun Peng, Rui Ma, Hongwei Qin, and Yan Wang. Elic: Efficient learned image compression with unevenly grouped space-channel contextual adaptive coding. *arXiv preprint arXiv:2203.10886*, 2022. **3**
- [22] Dailan He, Yaoyan Zheng, Baocheng Sun, Yan Wang, and Hongwei Qin. Checkerboard context model for efficient learned image compression. In *Proceedings of the IEEE/CVF Conference on Computer Vision and Pattern Recognition*, pages 14771–14780, 2021. **1**
- [23] Dzung T Hoang, Philip M Long, and Jeffrey Scott Vitter. Rate-distortion optimizations for motion estimation in low-bit-rate video coding. In *Digital Video Compression: Algorithms and Technologies 1996*, volume 2668, pages 18–27. SPIE, 1996. **4**
- [24] Qibin Hou, Ming-Ming Cheng, Xiaowei Hu, Ali Borji, Zhuowen Tu, and Philip HS Torr. Deeply supervised salient object detection with short connections. In *Proceedings of the IEEE conference on computer vision and pattern recognition*, pages 3203–3212, 2017. **2**
- [25] Andrew Howard, Mark Sandler, Grace Chu, Liang-Chieh Chen, Bo Chen, Mingxing Tan, Weijun Wang, Yukun Zhu, Ruoming Pang, Vijay Vasudevan, et al. Searching for mobilenetv3. In *Proceedings of the IEEE/CVF international conference on computer vision*, pages 1314–1324, 2019. **4**
- [26] Diederik P Kingma and Max Welling. Auto-encoding variational bayes. *arXiv preprint arXiv:1312.6114*, 2013. **1**

- [27] Jooyoung Lee, Seunghyun Cho, and Seung-Kwon Beack. Context-adaptive entropy model for end-to-end optimized image compression. *arXiv preprint arXiv:1809.10452*, 2019. **1**
- [28] Jooyoung Lee, Seunghyun Cho, and Munchurl Kim. An end-to-end joint learning scheme of image compression and quality enhancement with improved entropy minimization. *arXiv preprint arXiv:1912.12817*, 2019. **1**
- [29] Mu Li, Kede Ma, Jane You, David Zhang, and Wangmeng Zuo. Efficient and effective context-based convolutional entropy modeling for image compression. *IEEE Transactions on Image Processing*, 29:5900–5911, 2020. **1**
- [30] Chaoyi Lin, Jiabao Yao, Fangdong Chen, and Li Wang. A spatial rnn codec for end-to-end image compression. In *Proceedings of the IEEE/CVF Conference on Computer Vision and Pattern Recognition*, pages 13269–13277, 2020. **1**
- [31] Haojie Liu, Tong Chen, Peiyao Guo, Qiu Shen, Xun Cao, Yao Wang, and Zhan Ma. Non-local attention optimized deep image compression. *arXiv preprint arXiv:1904.09757*, 2019. **1**
- [32] Jiaheng Liu, Guo Lu, Zhihao Hu, and Dong Xu. A unified end-to-end framework for efficient deep image compression. *arXiv preprint arXiv:2002.03370*, 2020. **1**
- [33] Songtao Liu, Di Huang, et al. Receptive field block net for accurate and fast object detection. In *Proceedings of the European conference on computer vision (ECCV)*, pages 385–400, 2018. **4**
- [34] Changyue Ma, Zhao Wang, Ruling Liao, and Yan Ye. A cross channel context model for latents in deep image compression. *arXiv preprint arXiv:2103.02884*, 2021. **1**
- [35] Haichuan Ma, Dong Liu, Ning Yan, Houqiang Li, and Feng Wu. End-to-end optimized versatile image compression with wavelet-like transform. *IEEE Transactions on Pattern Analysis and Machine Intelligence*, 2020. **1**
- [36] Yi Ma, Yongqi Zhai, Chunhui Yang, Jiayu Yang, Ruo-fan Wang, Jing Zhou, Kai Li, Ying Chen, and Ronggang Wang. Variable rate roi image compression optimized for visual quality. In *Proceedings of the IEEE/CVF Conference on Computer Vision and Pattern Recognition*, pages 1936–1940, 2021. **2, 3**
- [37] Fabian Mentzer, George D Toderici, Michael Tschannen, and Eirikur Agustsson. High-fidelity generative image compression. *Advances in Neural Information Processing Systems*, 33:11913–11924, 2020. **2, 3**
- [38] David Minnen, Johannes Ballé, and George Toderici. Joint autoregressive and hierarchical priors for learned image compression. *arXiv preprint arXiv:1809.02736*, 2018. **1, 3**
- [39] David Minnen and Saurabh Singh. Channel-wise autoregressive entropy models for learned image compression. In *2020 IEEE International Conference on Image Processing (ICIP)*, pages 3339–3343. IEEE, 2020. **3**
- [40] Yash Patel, Srikar Appalaraju, and R Manmatha. Deep perceptual compression. *arXiv preprint arXiv:1907.08310*, 2019. **2, 3**
- [41] Yash Patel, Srikar Appalaraju, and R Manmatha. Saliency driven perceptual image compression. In *Proceedings of the IEEE/CVF Winter Conference on Applications of Computer Vision*, pages 227–236, 2021. **2**
- [42] Shibani Santurkar, David Budden, and Nir Shavit. Generative compression. In *2018 Picture Coding Symposium (PCS)*, pages 258–262. IEEE, 2018. **3**
- [43] Shuai Shao, Zijian Zhao, Boxun Li, Tete Xiao, Gang Yu, Xiangyu Zhang, and Jian Sun. Crowdhuman: A benchmark for detecting human in a crowd. *arXiv preprint arXiv:1805.00123*, 2018. **6**
- [44] Karen Simonyan and Andrew Zisserman. Very deep convolutional networks for large-scale image recognition. *arXiv preprint arXiv:1409.1556*, 2014. **3**
- [45] G Toderici, W Shi, R Timofte, L Theis, J Ballé, E Agustsson, N Johnston, and F Mentzer. Workshop and challenge on learned image compression. Available: <http://compression.cc/>, 2022. **5, 6**
- [46] Gregory K Wallace. The jpeg still picture compression standard. *IEEE transactions on consumer electronics*, 38(1):xviii–xxxiv, 1992. **1**
- [47] Jiayu Yang, Chunhui Yang, Yi Ma, Shiyi Liu, and Ronggang Wang. Learned low bit-rate image compression with adversarial mechanism. In *Proceedings of the IEEE/CVF Conference on Computer Vision and Pattern Recognition Workshops*, pages 140–141, 2020. **3**
- [48] Yibo Yang, Robert Bamler, and Stephan Mandt. Improving inference for neural image compression. *Advances in Neural Information Processing Systems*, 33:573–584, 2020. **1**
- [49] Richard Zhang, Phillip Isola, Alexei A Efros, Eli Shechtman, and Oliver Wang. The unreasonable effectiveness of deep features as a perceptual metric. In *Proceedings of the IEEE conference on computer vision and pattern recognition*, pages 586–595, 2018. **3, 4, 6**
- [50] Richard Zhang, Phillip Isola, Alexei A Efros, Eli Shechtman, and Oliver Wang. The unreasonable effectiveness of deep features as a perceptual metric. In *Proceedings of the IEEE conference on computer vision and pattern recognition*, pages 586–595, 2018. **6**
- [51] Jing Zhao, Bin Li, Jiahao Li, Ruiqin Xiong, and Yan Lu. A universal encoder rate distortion optimization framework for learned compression. In *Proceedings of the IEEE/CVF Conference on Computer Vision and Pattern Recognition*, pages 1880–1884, 2021. **1**

Supplementary

Super-High-Fidelity Image Compression via Hierarchical-ROI and Adaptive Quantization

Jixiang Luo
Sensetime Research

luojixiang@sensetime.com

Yan Wang
Tsinghua University

wangyan@air.tsinghua.edu.cn

Hongwei Qin
Sensetime Research

qinhongwei@sensetime.com

1. Dataset Detail

To reproduce our results, we list the subset of CrowdHuman testing dataset as shown in Tab. 1, where w , h are the width and height, and resolution varies from 615×461 to 4214×2730 . Besides, it consists of numerous people with various gestures and facial expression, which is more close to real situation. Different from Kodak and CLIC2002 testing dataset, its image format is JPEG and its quality is relatively inferior because of information loss and JPEG compression noise. However JPEG is the most popular format for transmission or storage, thus our experiment setting is more practical for industrial application.

2. Qualitative Results

We compare the original image, reconstructions from BPG, ELIC, HiFiC and ours(H-ROI) with regard to visual quality along with bpp, objective metrics PSNR and MS-SSIM, and subjective index LPIPS. We select images from Kodak dataset, CLIC2022 testing dataset and a subset of CrowdHuman testing dataset. The last row is the detail for local area of BPG, ELIC, HiFiC and H-ROI.

With the combination of PSNR, MS-SSIM, LPIPS, and the visual quality from human eyes using FastStone¹, the reconstructions from our methods are more pleasurable with regard to other methods. Fig. 1 and Fig. 2 depict the working diagram of FastStone, and it can zoom the picture in or out for all pictures with the same scale. Thus we can evaluate the smallest region such as 20×20 for width and height to distinguish which details have been missing or which structure is more complete. Besides, for the following visual comparisons, the last row marked with BPG, ELIC, HiFiC, H-ROI is captured by FastStone for a small region. Moreover, we evaluate the image from global to local perspective with FastStone.

In Fig. 3 and Fig. 4, we achieve the lowest LPIPS and comparable MS-SSIM and PNSR for HiFiC in CLIC2022 testing dataset and the subset of CrowdHuman testing dataset. Thus our methods occupy the merit of general-

Table 1. Subset of CrowdHuman

name	w	h
1066405,218a700048baf6a5	1024	683
1066405,22995000cde69f78	840	440
1066405,239eb000e5646ae4	1024	768
1066405,245c90002f8426d4	1024	512
1066405,278c500023fc022b	1280	720
1066405,291b00006e60dcd4	800	431
1066405,295ee0009ddeb8c	980	653
1066405,3160004fdd79b1	1497	998
1066405,45222000bb360294	550	367
1066405,50791000dde5fe22	1024	679
1066405,5187000bbd15ae1	1980	1485
1066405,686000d3439407	2000	1333
1066405,8788c000723bb59d	1000	667
1066405,8921c00054293f10	300	450
1066405,9006e0007cd7a2ab	1700	1131
1066405,91c07000feb183c9	300	470
1066405,c264200072c9b890	640	458
1066405,caf4c00088060824	2000	1308
1066405,cbb81000e1b4a4a6	2400	1600
1066405,cda8500076abec04	2048	1174
1066405,ce1710005ce68455	3180	2204
1066405,ceb8c000c098b409	3264	2448
1066405,cedc80008a06a63c	3238	2850
1066405,ceedc000dc09b8e1	1024	683
1066405,d050008daf0bde	900	675
1066405,d583000a00e73e2	4214	2730
1066405,db19000e046d964	800	600
1066405,dd9b000d31071df	615	461
1066405,e77810002028a57e	1500	1125
1066405,e9ec100081152e8c	1600	2397

ization from small resolution 512×768 or 615×461 to larger resolution 4124×2730 . Our method has the smallest bit consumption, but achieves comparable or better visual quality for face, text or other textures. Besides, we maintain the detail of other regions as shown in the following

¹<https://www.faststone.org/>

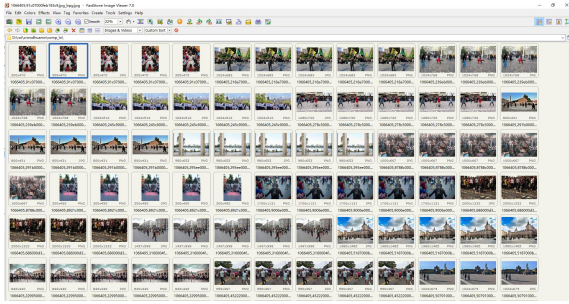


Figure 1. The overall of folder in FastStone.

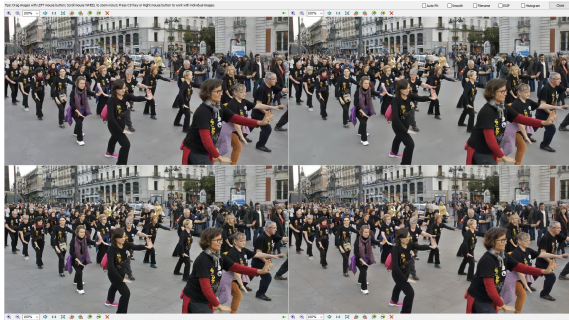


Figure 2. Compare pictures at the same screen with maximal number of 4 in FastStone.

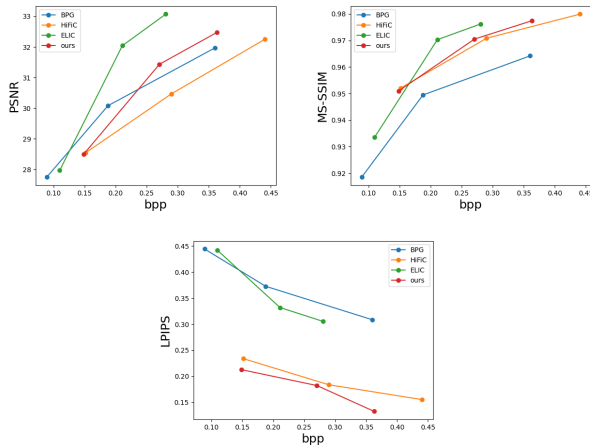


Figure 3. Performance on PSNR, MS-SSIM and LPIPS of our method, HiFiC, ELIC and BPG on CLIC2022 testing dataset.

visualization.

3. Object Codec

We further study the objective coding via mask for latents, then we can reconstruct the region of interests. We visualize more reconstruction from only a part of latents corresponding to certain objects. The top row in Fig. 5,

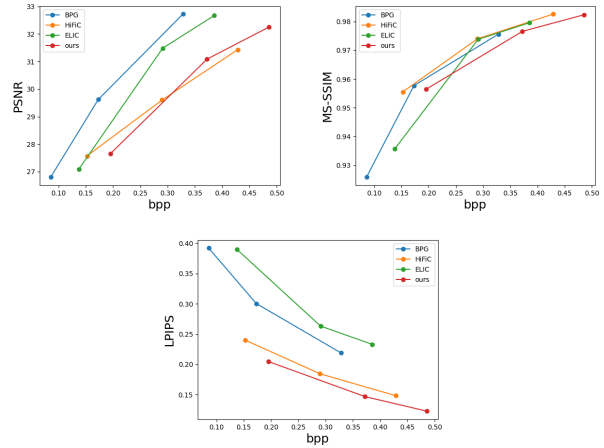


Figure 4. Performance on PSNR, MS-SSIM and LPIPS of our method, HiFiC, ELIC and BPG on subset of CrowdHuman testing dataset.

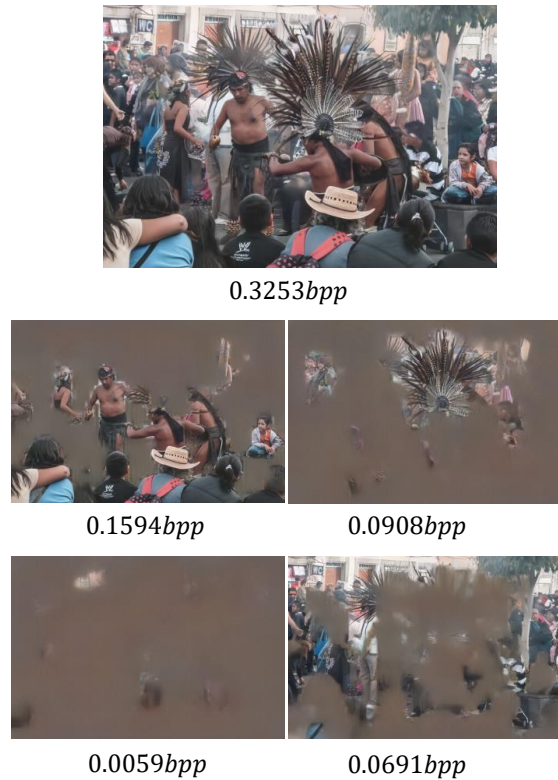


Figure 5. Reconstruction for objective coding

Fig. 6 and Fig. 7 is the complete reconstruction. The left rows are the partial reconstruction from the part of channels. To be specific, we calculate the bpp of each part, and the sum of bpp in part channels is equal to the total bpp.



0.3829bpp



0.3829bpp

0.0176bpp



0.0112bpp

0.0333bpp

Figure 6. Reconstruction for objective coding

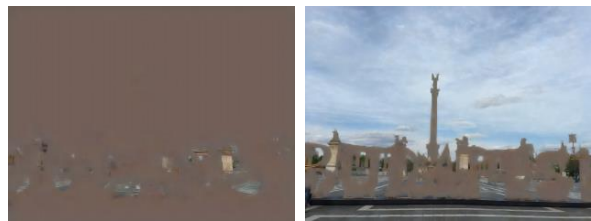


0.1160bpp



0.0739bpp

0.0051bpp



0.0067bpp

0.0304bpp

Figure 7. Reconstruction for objective coding



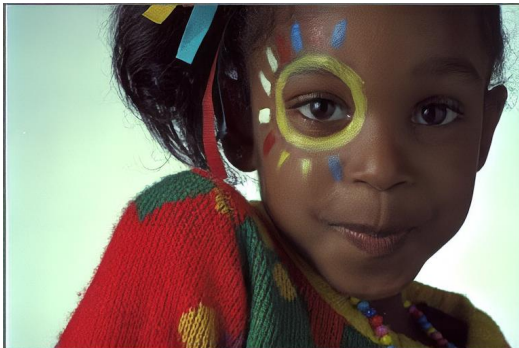
origin



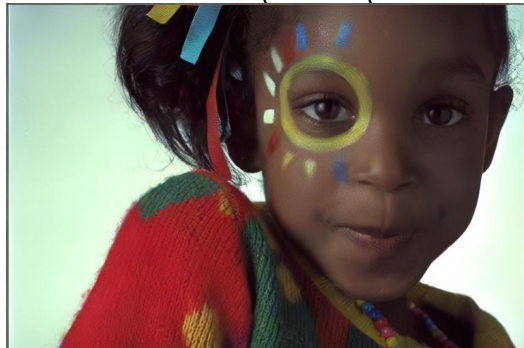
BPG: 0.2491bpp
32.9533\0.9618\0.3076



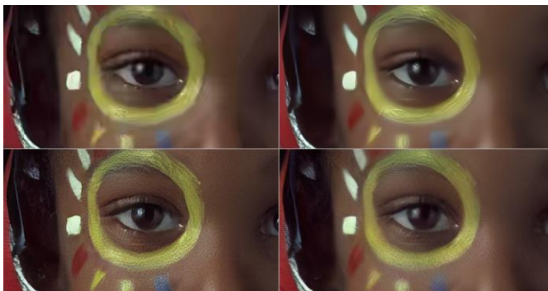
ELIC: 0.1111bpp
31.3842\0.9514\0.3832



HiFiC: 0.1412bpp
29.3052dB\0.9481\0.2305



H-ROI: 0.1056bpp
29.1097dB\0.9401\0.2144



BPG\ELIC
HiFiC\H-ROI



BPG\ELIC
HiFiC\H-ROI



origin



*BPG: 0.5345bpp
32.5087\0.9800\0.2064*



*ELIC: 0.2713bpp
28.3027dB\0.9405\0.3536*



*HiFiC: 0.2219bpp
24.7218dB\0.9169\0.2732*



*H-ROI: 0.2214bpp
25.5379dB\0.9094\0.2399*



*BPG\ELIC
HiFiC\H-ROI*



*BPG\ELIC
HiFiC\H-ROI*



origin



*BPG: 0.5345bpp
32.5087\0.9800\0.2064*



*ELIC: 0.2599bpp
29.5971dB\0.9755\0.2503*



*HiFiC: 0.2057bpp
25.1815dB\0.9675\0.2314*



*H-ROI: 0.1902bpp
26.0917dB\0.9659\0.1904*



*BPG\ELIC
HiFiC\H-ROI*



*BPG\ELIC
HiFiC\H-ROI*



origin



BPG: 0.4162bpp
32.1874\0.9518\0.2579

ELIC: 0.1593bpp
30.3688dB\0.9518\0.3677



HiFiC: 0.1503bpp
27.5128dB\0.9456\0.2292

H-ROI: 0.1269bpp
28.5816dB\0.9365\0.2176



BPG\ELIC
HiFiC\H-ROI

BPG\ELIC
HiFiC\H-ROI



origin



BPG: 0.2559bpp
31.8326\0.9658\0.3277



ELIC: 0.1423bpp
31.4854dB\0.9644\0.3710



HiFiC: 0.1288bpp
29.2904dB\0.9557\0.2332



H-ROI: 0.1276bpp
29.1456dB\0.9562\0.2080



BPG\ELIC
HiFiC\H-ROI



BPG\ELIC
HiFiC\H-ROI



origin



BPG: 0.3636bpp
34.4844\0.9833\0.1327



ELIC: 0.1607bpp
31.6558dB\0.9724\0.2123



HiFiC: 0.2057bpp
30.4797dB\0.9741\0.1851



H-ROI: 0.1596bpp
29.3404dB\0.9692\0.1830



BPG\ELIC
HiFiC\H-ROI



BPG\ELIC
HiFiC\H-ROI



origin



BPG: 0.5091bpp
32.6204\0.9777\0.2048



ELIC: 0.1936bpp
30.1614dB\0.9692\0.2795



HiFiC: 0.2175bpp
27.2225dB\0.9644\0.2413



H-ROI: 0.1785bpp
27.6046dB\0.9660\0.2148



BPG\ELIC
HiFiC\H-ROI



BPG\ELIC
HiFiC\H-ROI



origin



BPG: 0.4948bpp
32.0291\0.9797\0.2219



ELIC: 0.2103bpp
30.0590dB\0.9685\0.2896



HiFiC: 0.2193bpp
27.4258dB\0.9631\0.2510



H-ROI: 0.2021bpp
27.6427dB\0.9589\0.2154



*BPG**ELIC*
*HiFiC**H-ROI*



*BPG**ELIC*
*HiFiC**H-ROI*



origin



*BPG: 0.1073bpp
36.5704\0.9810\0.3250*



*ELIC: 0.0898bpp
35.1176dB\0.9785\0.3979*



*HiFiC: 0.2199bpp
33.6874dB\0.9731\0.2521*



*H-ROI: 0.0782bpp
32.1564dB\0.9742\0.2264*



*BPG\ELIC
HiFiC\H-ROI*



*BPG\ELIC
HiFiC\H-ROI*



origin



BPG: 0.0756bpp
39.1132\0.9825\0.1871



ELIC: 0.0529bpp
37.3495dB\0.9782\0.2789



HiFiC: 0.1453bpp
37.4245dB\0.9812\0.2067



H-ROI: 0.0627bpp
34.0022dB\0.9798\0.1936



BPG\ELIC
HiFiC\H-ROI



BPG\ELIC
HiFiC\H-ROI